CRUISE AERODYNAMICS OF USB

NACELLE/WING GEOMETRIC VARIATIONS*

John A. Braden, John P. Hancock, and Kenneth P. Burdges
Lockheed-Georgia Company

SUMMARY

Experimental results are presented on aerodynamic effects of geometric variations in USB nacelle configurations at high-speed cruise conditions. Test data includes both force and pressure measurements on two- and three-dimensional models powered by upper-surface blowing nacelles of varying geometries. Experimental results ure provided on variations in nozzle aspect ratio, nozzle boattail angle and multiple-nacelle installations. The nacelles are ranked according to aerodynamic drag penalties as well as overall installed drag penalties. Sample effects and correlations are shown for data obtained with the pressure model.

INTRODUCTION

Use of upper surface blowing (USB) engine installations, illustrated in figure 1, has been demonstrated as a viable means of STOL high-lift augmentation by both industry and government sponsored research over the past several years. Such studies have shown the system to be attractive for STOL application from a number of viewpoints. These include generally favorable acoustic characteristics for the terminal area environment, reasonably practical structural compatibility with the airframe, and acceptable flexibility for integrating with basic operational systems or sub-systems. These, of course, are in addition to the recognized potential for good STOL performance. in contrast to the low-speed accountability of the USB system, a comparable data base for the high-speed cruise regime has been lacking. To fill this need, the Lockheed-Georgia Company, under contract to the NASA, has conducted experimental investigations wherein USB nacelle/wing geometries and operating conditions are systematically varied in the $0.5 \leq M_o \leq 0.8$ cruise regime. The basic goal of this parametric investigation is to define those geometric properties and operating conditions indicative of minimum cruise-drag penalties and from which more refined USB configurations can evolve.

The present paper provides a brief over-view of the experimental program, currently still in progress, along with preliminary findings believed to be of general interest. The experimental work encompasses force-test evaluations, surface pressure measurements, and wake surveys behind powered configurations. A companion analytical effort is involved in the basic program, but an evaluation of math model capabilities via experimental correlation must await a more thorough examination of the test results.

SYMBOLS

Values are given in both SI and U.S. Customary Units. The measurements and calculations were made in U.S. Customary Units.

A_N	nozzle exit area, cm^2 (in^2)
AR	nozzle aspect ratio, w^2/A_N
b/2	wing semispan, cm (in.)
c	wing chord, cm (in.)
C_L	lift coefficient
C_μ	thrust coefficient
ΔC_D	incremental drag coefficient
D	drag, N (lb)
H	nozzle stagnation pressure, N/m^2 (lb/in^2)
H/P_o	nozzle pressure ratio
M_o	freestream Mach number
P_o	freestream static pressure, N/m^2 (lb/in^2)
q_o	freestream dynamic pressure, N/m^2 (lb/in^2)
S	wing area per semispan, cm^2 (in^2)
T	gross thrust, N (lb)

w	nozzle width, cm (in.)
X	chordwise distance from wing leading edge, cm (in.)
α	angle of attack, deg
β	boattail angle, deg
δ_i	jet turning angle measured statically, deg
η	thrust efficiency for wing/nacelle combination, T_{MEAS}/T_{ISOL}

Subscripts:

A, Aero	aerodynamic
F	friction
INT	interference
ISOL	isolated
l	local
M, MEAS	measured
N	nacelle
TOT	total

EXPERIMENTAL OBJECTIVES

The objective of this experimental program is to establish a transonic experimental data base covering a wide variation of nacelle geometric parameters. An extensive array of nacelle/wing geometric configurations were developed so that experimental evaluation of the transonic force and surface pressure characteristics could be made. The geometric configurations were tested over a wide range of Mach number, angle of attack, and nozzle pressure ratio to establish an extensive data base from which summary "effects" are developed. The primary geometric variations in nacelle configurations, illustrated in figure 2, for which aerodynamic "effects" data are generated and aerodynamically ranked are:

o   nozzle exit aspect ratio

o   nozzle boattail angle

167

o   chordwise/vertical/spanwise positioning

o   size and number of nacelles

Secondary experimental objectives include the effects of:

o   wing sweep

o   wing camber modifications

o   inlet flow-field effects

o   jet deflectors

o   wing/nacelle filleting and streamlining

For the present discussion, only selected combinations of these geometric variations will be considered. In particular, nozzle aspect ratio, boattail angle and multiple-nacelle interference will be covered.

CFF TUNNEL TESTS

Test Facility

The experimental program is being conducted in the Lockheed-Georgia Compressible Flow Facility (CFF), which is a variable porosity, blowdown wind tunnel (figure 3). Operating ranges are 0.2 to 1.2 Mach number and up to 164×10^6/M Reynolds number in the transonic speed range. The test section, which is 50.8 cm (20 in.) wide, 71.1 cm (28 in.) high and 182.9 cm (72 in.) long, can be equipped with porous or solid walls to match particular test requirements. Model engine air supply is provided by an independent 2.068 MN/m^2 (300 lb/in^2) source. For powered force testing, air is supplied to the model through the force balance by a bellows arrangement.

Test Conditions

The Mach number range of interest in the experimental effort is $0.5 \leq M_o \leq 0.70$ to the unswept wing and $0.6 \leq M_o \leq 0.80$ for the swept wing model. Maximum nozzle pressure ratios (H/P_o) up to about 3.0 were tested over most of these speed ranges. Model angle of attack was varied from 0 degrees to 5 degrees encompassing all normal cruise settings. Flow visualization using titanium dioxide combined with oil was employed extensively to help understand the force and pressure test results.

Models

The test configurations are composed of a large number of interchangeable nozzles that fit the basic wing. There are two basic wings, swept and unswept, which have a removable tip allowing conversion from 2-D to 3-D configurations. The two-dimensional pressure models span the 50.8 cm (20 in.) horizontal width of the tunnel. For 3-D force testing, the wing is mounted vertically on the balance system in the tunnel floor. The semi-span-wing (b/2 = 50.8 cm (20 in.)) then spans 70 percent of the tunnel height (71.1 cm (28 in.)). Examples of the two force models, which illustrate unswept and swept 3-D wings, are provided in figures 4 and 5, respectively.

Figure 6 illustrates the build-up of a two-dimensional pressure model, using the un-swept wing, along with the traversing wake rake. A supercritical-type of wing section is used for both the unswept and 25 degree swept wing. This airfoil section has a streamwise thickness ratio of 16 percent for the unswept wing application and 14 percent for the swept wing case; the wing chord is 17.8 cm (7 in.) in both instances. The wing design Mach numbers are about 0.7 and 0.8, respectively.

As illustrated, the nozzle air supply at 2.068 MN/m^2 (300 lb/in^2) is routed through the underwing duct and into a plenum formed by a faired-over forebody. The air is exhausted through a choke plate and exits from the nozzle at pressure ratios (H/P$_0$) ranging up to a maximum of 3.0. The same forebody is used with a number of interchangeable nozzles which have different exit shapes, but the same discharge area. Unpowered configurations may be bui t up by substitution of a flow-through inlet for the faired forebody.

Model instrumentation includes surface pressure taps at 5 spanwise positions on the wing and along the nozzle upper surface. A traversing wake rake provides the capability for sampling jet profiles and for evaluating momentum losses in the wing/nacelle wake.

RESULTS AND DISCUSSION

The force-test phase of the experimental program has recently been completed and pressure testing is currently in progress. For this reason, the present discussions emphasize force test results with limited reference to pressure testing, except where available data permits.

Aerodynamic Ranking

Following the convention established in low-speed, high-lift practice, the measured lift and accelerating force may be sub-divided into assumed components as shown in figure 7. The direct, or reactive thrust terms, $\eta C_\mu \sin (\alpha + \delta_i)$ and $\eta C_\mu \cos (\alpha + \delta_i)$ are removed from the measured data and the assumption made that the remainder represents the interactive

169

aerodynamic force and moment on the combined wing/nacelle. It is implicit in this approach that the statically determined thrust efficiency, η, representing scrubbing and vectoring losses, and turning angle, δ_i, are invariant with forward speed. It should also be noted that the loss represented by $(1 - \eta)$ is a constant increment of gross thrust and a much higher percentage of net thrust. The relationship between gross and net thrust is shown in figure 7.

Following the convention just discussed while holding constant circulation lift ($C_{L_A} = 0.40$) and Mach number (0.68), a comparison has been made of the aerodynamic interference drag for a D-duct nozzle to an AR = 6 nozzle, as shown in figure 8. Based on these aerodynamic interference drag levels, the wide (AR = 6) nozzle is superior to the semi-circular (D-duct) nozzle. However, this apparent aerodynamic advantage is gained at the expense of much greater penalty in scrubbing losses as indicated by the efficiencies shown at the top of the figure.

To obtain a more realistic ranking of these nozzles, a total interference drag coefficient is obtained by adding back in the losses associated with the assumed vectoring:

$$\left(\Delta C_{D_{INT}} \right)_{TOT} = \left(\Delta C_{D_{INT}} \right)_{AERO} + C_\mu \left[1 - \eta \cos (\alpha + \delta_i) \right]$$

This coefficient is compared in figure 9 for the same semi-circular and wide rectangular nozzles. In this comparison the semi-circular nozzle has the lowest drag. The magnitudes and rankings of these coefficients correspond to those which would be obtained by working only with the measured accelerating force reduced by the calibrated, isolated nacelle thrust and the clean wing/body drag plus nacelle friction. Therefore, ranking the nozzle geometric parameters in terms of the total interference drag rather than the aerodynamic drag alone is a basic process used throughout the present study.

Effect of Nozzle Aspect Ratio

· r characteristic exit shapes, three of which are illustrated in figure 10, form the basic variation in nozzle aspect ratio. The fourth shape is an aspect ratio 4 nozzle. This family of nozzles is designed with low boattail angles ($6^\circ - 12^\circ$) to prevent the effect of boattail angle from obscuring the true aspect ratio effects. Interference drag coefficients, which are inclusive of scrubbing losses and normalized to the drag of the circular nozzle are shown in figure 11. The Mach number and lift coefficients represent typical cruise conditions near the drag-rise Mach number of the unswept wing/nacelle combination. The pressure ratios (H/P_o) ranging from 1.85 - 2.55 are nozzle pressure ratios; corresponding fan pressure ratios for the indicated cruise conditions would be 1.36 - 1.88. The data shown in figure 11 show a pronounced drag advantage for the "D-duct" configuration. It is believed from preliminary analysis that this advantage stems from a lack of nozzle side flair and more rounded corners near the exit while simultaneously deriving some benefit through lift augmentation.

170

The better lift-generation capability of the wide nozzles is demonstrated in figure 12, which compares total lift across the pressure ratio range at typical cruise conditions of a constant angle of attack of 3 degrees and Mach number of 0.68. A comparison of the lift with clean wing values at the corresponding angle of attack shows that the circular nozzle provides very little lift augmentation, while the wide nozzles provide lift augmentation considerably in excess of the jet-supported lift. In fact, lift augmentation on the order of 3 to 5 times the direct lift due to thrust has been found to be characteristic of the wider nozzles. The "D-duct" generates lift augmentation ratios of about 2.5 at maximum blowing levels.

Effect of Boattail Angle

A second set of medium sized nozzles, spanning the aforementioned aspect ratio range, but characterized by high boattail angles (17° - 35°), is available in the model matrix. With the effect of nozzle aspect ratio on drag known from the previous evaluation, the effect of boattail angle on total interference drag may be determined. Figure 13 shows these results with the data again normalized to the circular nozzle drag. In the pressure ratio range 2.20 - 2.60, the maximum useable boattail angle appears to be about 20 - 21 degrees. There is an indication that the onset of boattail separation is delayed slightly at high blowing rates by the pumping action of the jet. The separated flow pattern near the exit of the aspect ratio 4 nozzle with a 35 degree boattail angle is shown in figure 14.

Effect of Multiple Nacelles

Both two- and four-engine nacelle configurations were tested on the swept wing. Figure 15 illustrates the increase in total interference drag for the four-engine airplane as compared to that obtained for twin-engine configurations tested separately with nacelles located at inboard and outboard wing positions. Although the nacelles are about 2 nacelle diameters apart, the increase in total interference drag is around 0.004, or equivalent to the drag of a single nacelle at low blowing levels. This drag diminishes by about 50% at the higher C_μ values. The interference drag also appears to be relatively insensitive to Mach number near the drag rise as indicated in the figure.

Pressure Test Results

A typical USB-pressure model is shown on figure 16 as mounted in the CFF. A sampling of data obtained with the traversing wake rake behind a circular nozzle is provided in figure 17. The basic effect of the wing on the jet cross section is seen to be a downward displacement of the contours as the jet tends toward wing attachment. Acquisition of similar data, both statically and wind-on, are in progress with nacelles of various shapes and sizes.

171

Additional results from the pressure tests are provided in figure 18. Wing surface pressures along the jet centerline of a D-duct nacelle are compared with results from a powered vortex-lattice modeling technique. The correlations afforded by the theoretical program and the pressure test results are providing significant insight into the aerodynamics of the USB system.

CONCLUSIONS

Based on preliminary evaluations of both force and pressure measurements obtained in the USB-Cruise experimental program, the following conclusions have been drawn:

o   The semi-circular ("D-duct") nozzle is superior from the standpoint of the total installed drag penalty to either the circular nozzle or the wide (high aspect ratio) nozzles.

o   Boattail angles of 20-21 degrees are permissible without large drag penalties.

o   Tests of two adjacent nacelles have indicated the presence of an additional interference drag penalty, which amounts to about 25 percent of the total interference drag of the two nacelles tested separately.
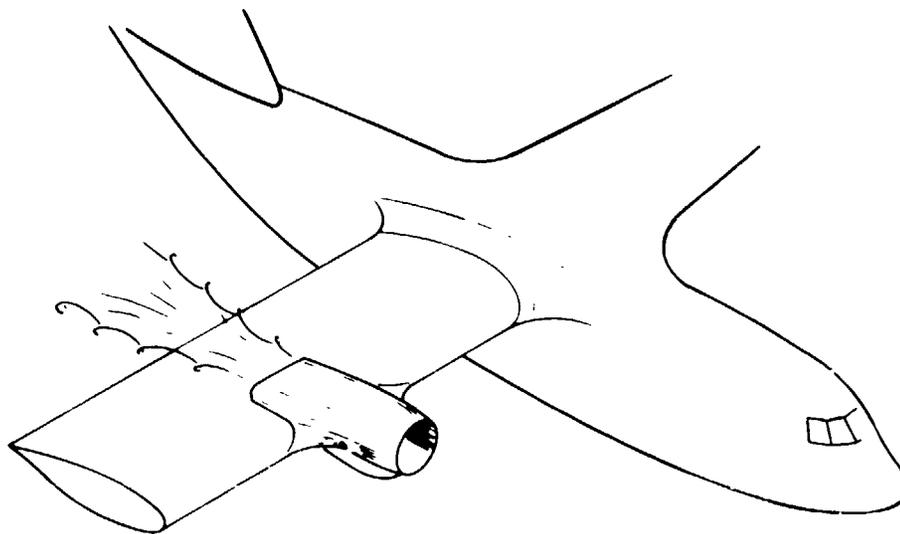
Figure 1.- Aerodynamic effects of USB nacelle/wing
geometric variations.

SPANWISE & CHORDWISE POSITION
NOZZLE ASPECT RATIO & BOATTAIL

WING SWEEP & CAMBER

PYLON HEIGHT
SIZE & NUMBER OF ENGINES
INLET FLOW FIELD
NOZZLE DEFLECTOR
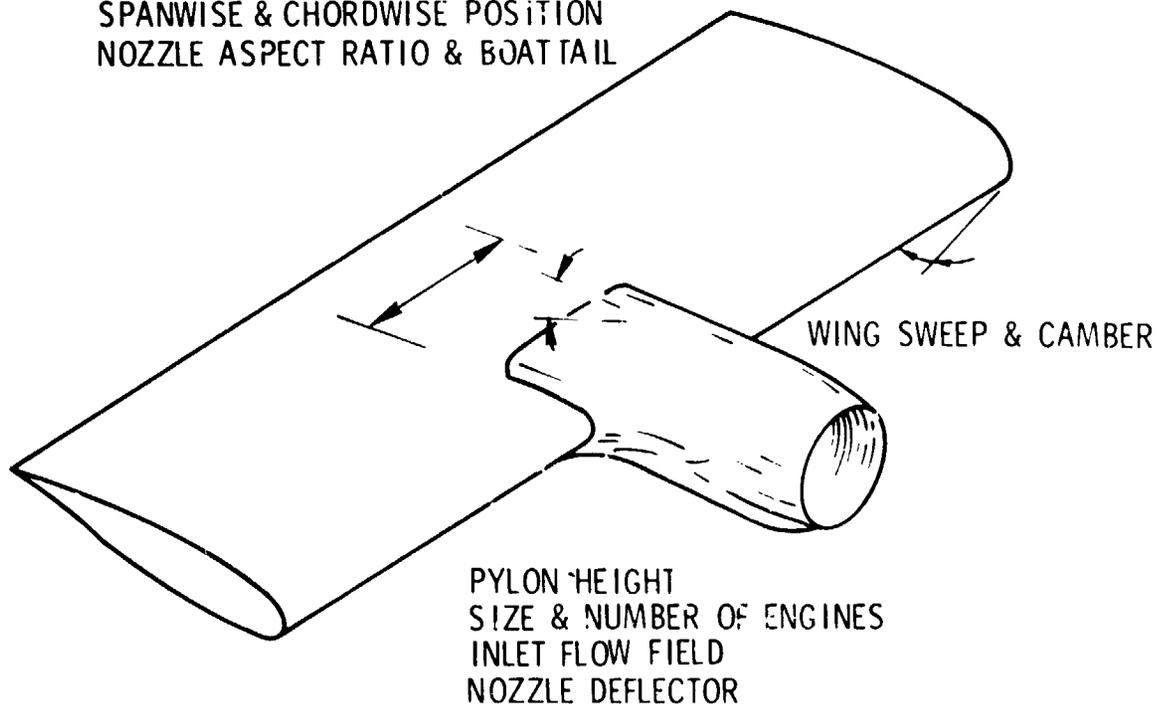
Figure 2.- Geometric effects.   2-D and 3-D.

173
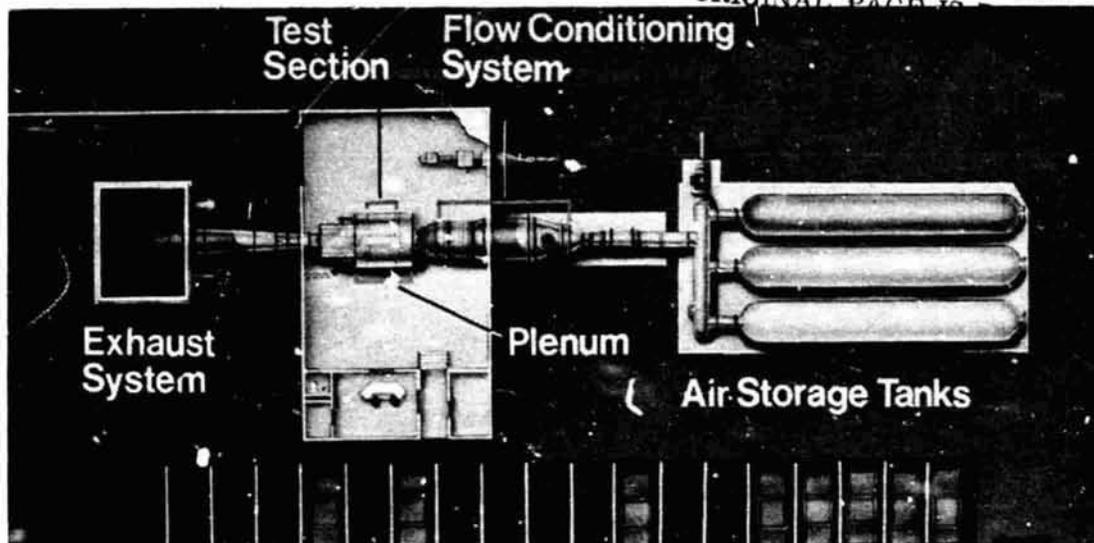
Figure 3.- Lockheed Compressible Flow Facility. Transonic blowdown tunnel $(0.2 \leq M_O \leq 1.2)$; Reynolds number capability of $164 \times 10^6/m$; variable wall porosity; model blowing capability of 2.068 MN/m^2 $(300$ lb/in$^2)$.
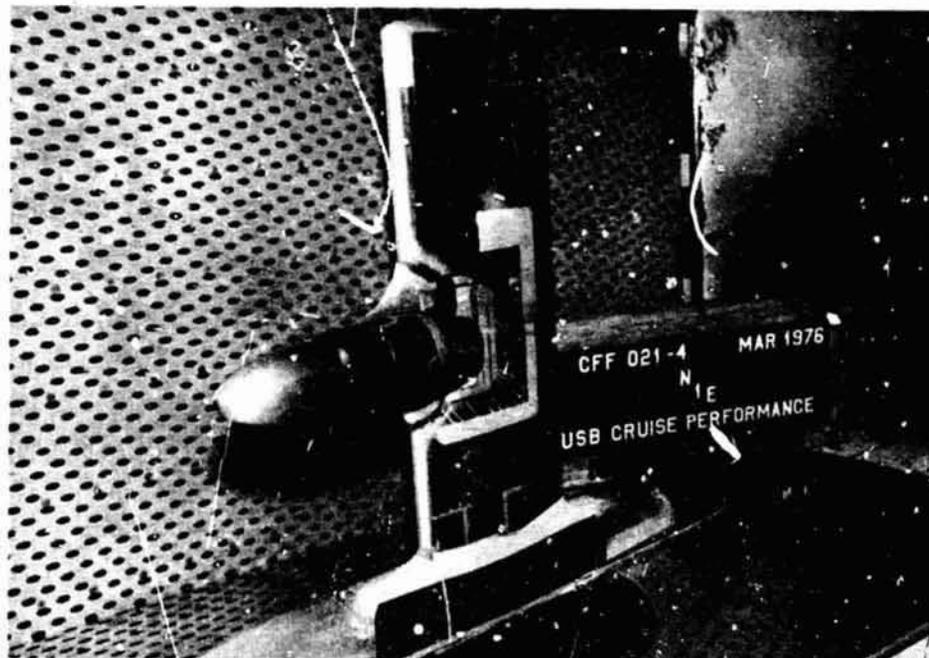
Figure 4.- 3-D unswept model.

CFF 020   FEB 1976
$F_2W_2B_{5,6}P_{9,10}C_{3,4}N_{8,2}$
USB CRUISE PROGRAM

Figure 5.- 3-D swept model.

Nacelle Exit Nozzle — Choke Plate

Mid Pylon

Nacelle Forebody

Wake Rake

Nacelle Air Supply

Removable Airfoil Tip

Straight Wing with Static Pressure Orifices

Aft Pylon Fairing
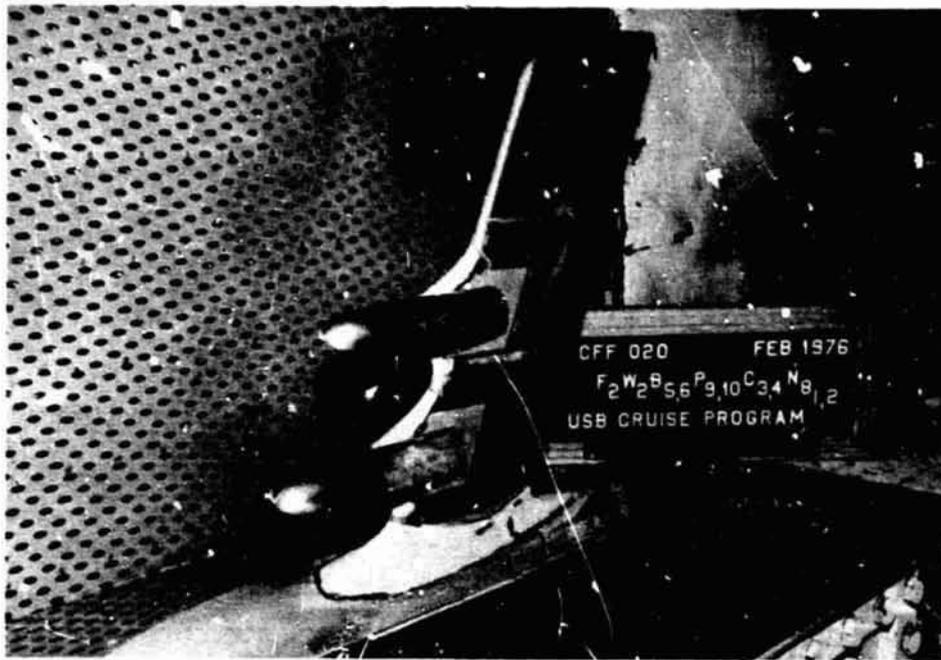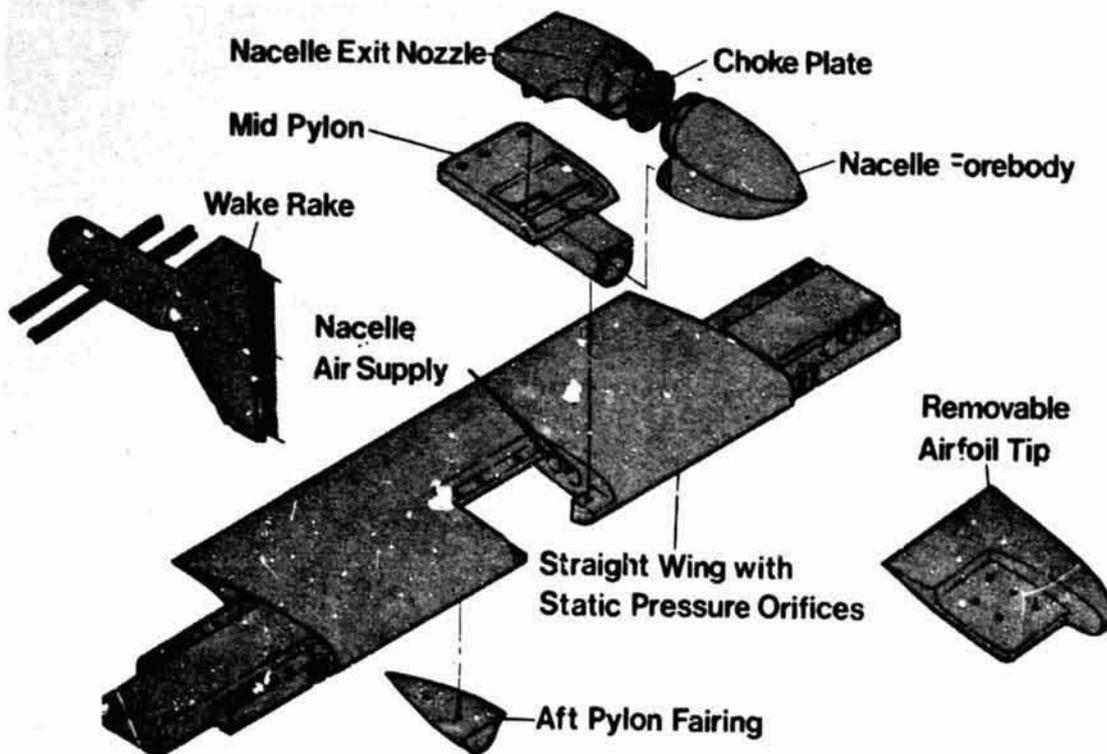
Figure 6.- Typical test model.

$$\Delta C_{D_{TOT}} = \Delta C_{D_N} + C_\mu \left[1 - \eta\cos(\alpha + \delta_j)\right]$$

$$\Delta C_{D_N} = \Delta C_{D_{INT}} + \Delta C_{D_F}$$
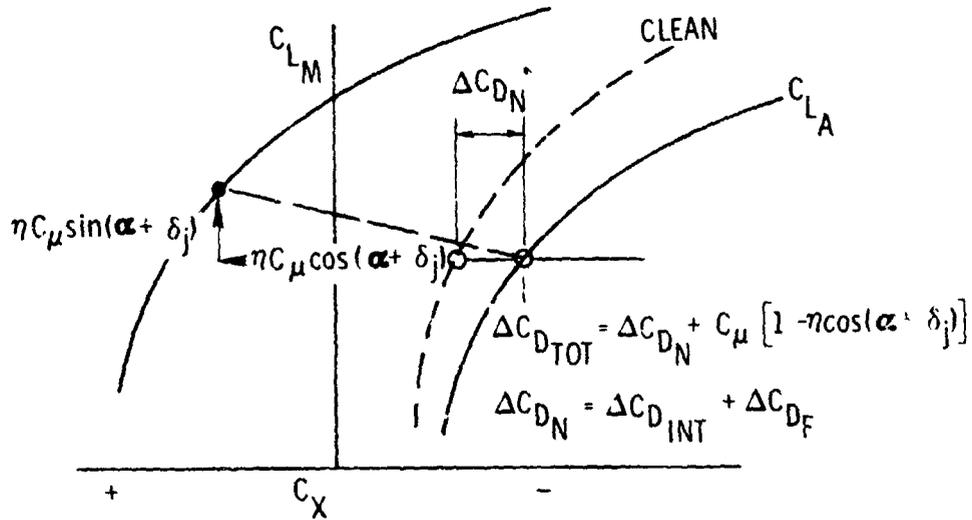
- ALL NOZZLES CALIBRATED ISOLATED
- δ_{jet}, EFFICIENCY (η) FROM STATIC WING + NACELLE CALIBRATION
- NET THRUST = GROSS THRUST - RAM DRAG

Figure 7.- Drag increment definition (C_X represents all coefficients shown).

	NACELLE	η	δ_j	AR	SHAPE
O	A	.97	7^0	2.5	
□	B	.89	12^0	6.0	
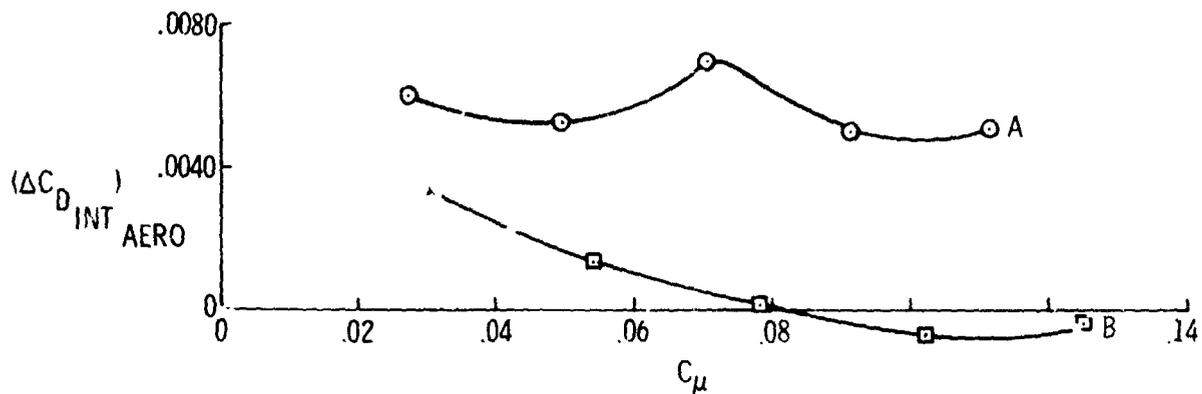
Figure 8.- Nacelle ranking; aerodynamic interference drag.

NACELLE	η	δj	AR	SHAPE
○ A	.97	7^0	2.5	⌒
□ B	.89	12^0	6.0	⬭
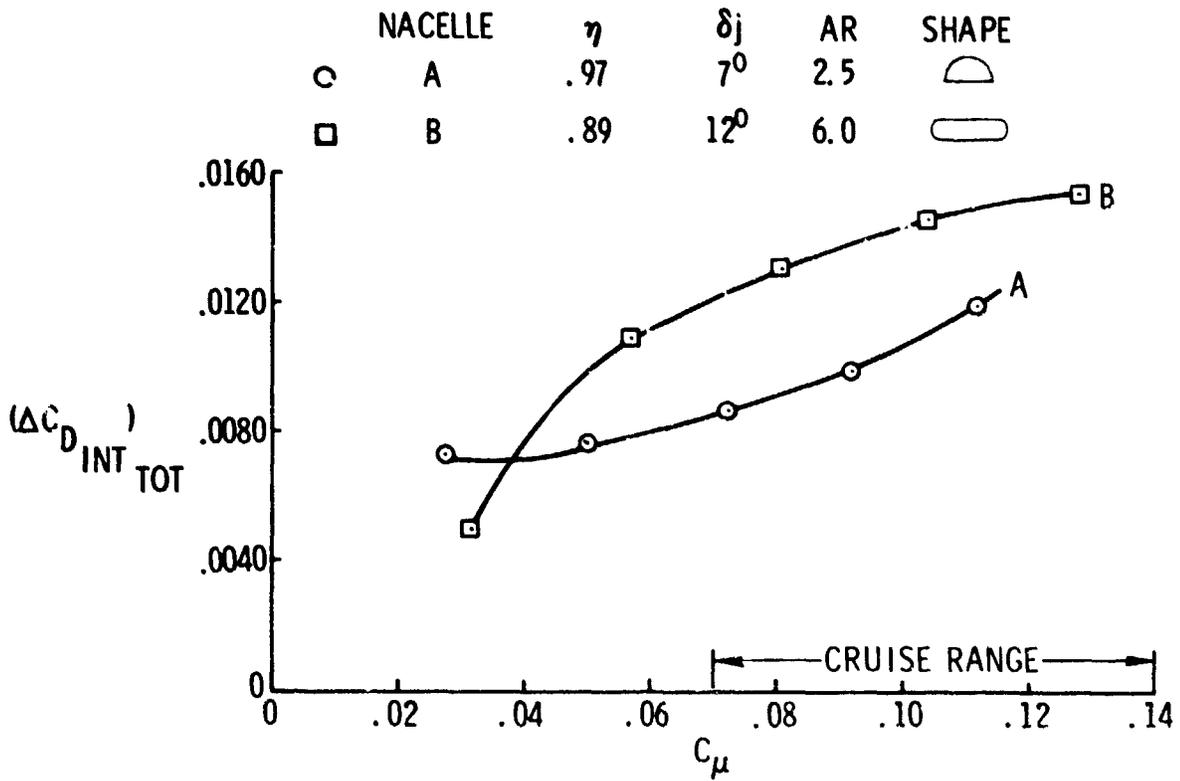
Figure 9.- Nacelle ranking; total interference drag.
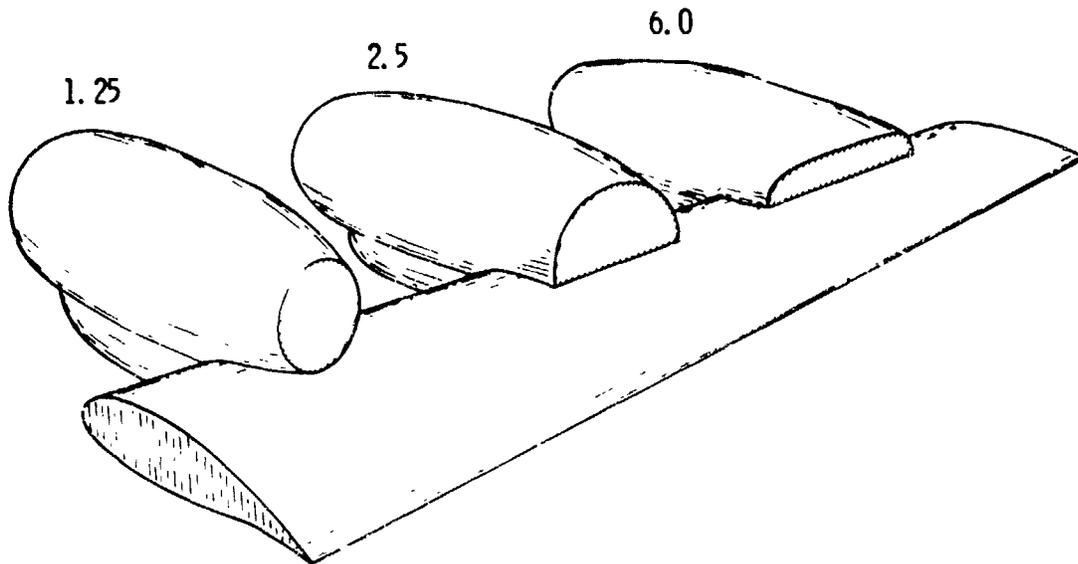
Figure 10.- Nozzle aspect ratio variation; $6^0 \leq \beta \leq 12.5^0$.

177

$$\frac{(\Delta C_{D_{INT}})_{TOT}}{(\Delta C_{D_{INT}})_{TOT_{AR = 1.25}}}$$

H/P₀

—⊙— ≈ 1.85
---□--- ≈ 2.20
—·△·— ≈ 2.55
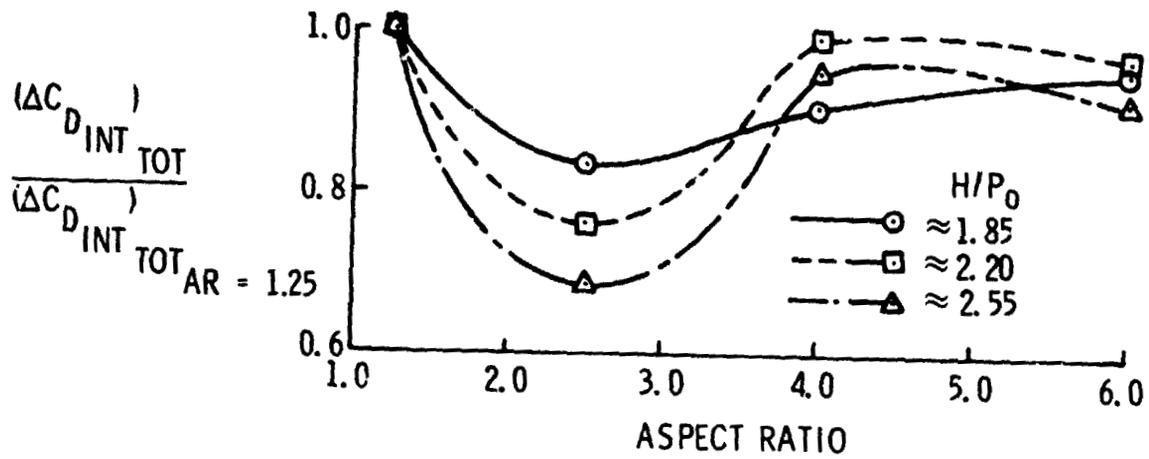
ASPECT RATIO

Figure 11.- Effect of nozzle aspect ratio on nacelle drag.
Unswept wing; $M_O = 0.68$; $C_{L_A} = 0.40$.

NOZZLE
ASPECT
RATIO

$a = 3^0$

CLEAN
WING

$C_{L_{TOT}}$

6
4
2.5
1.25

H/P₀
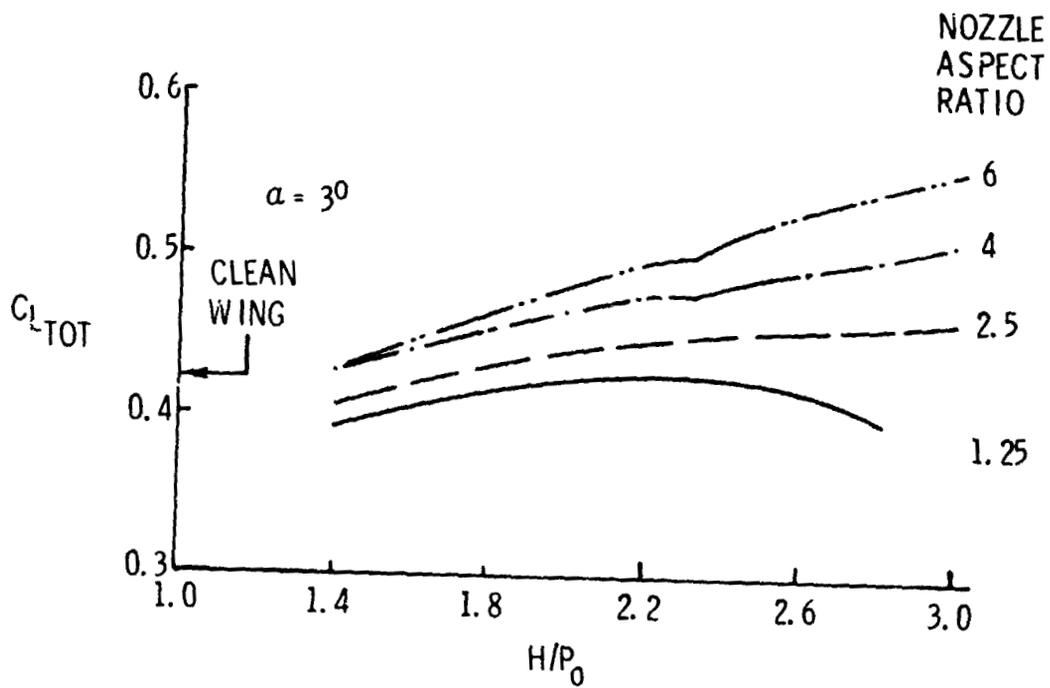
Figure 12.- Effect on total lift of nozzle aspect ratio variation.
Unswept wing; $M_O = 0.68$.

$$\frac{(\Delta C_{D_{INT}})_{TOT}}{(\Delta C_{D_{INT}})_{TOT_{\beta=6}}}$$
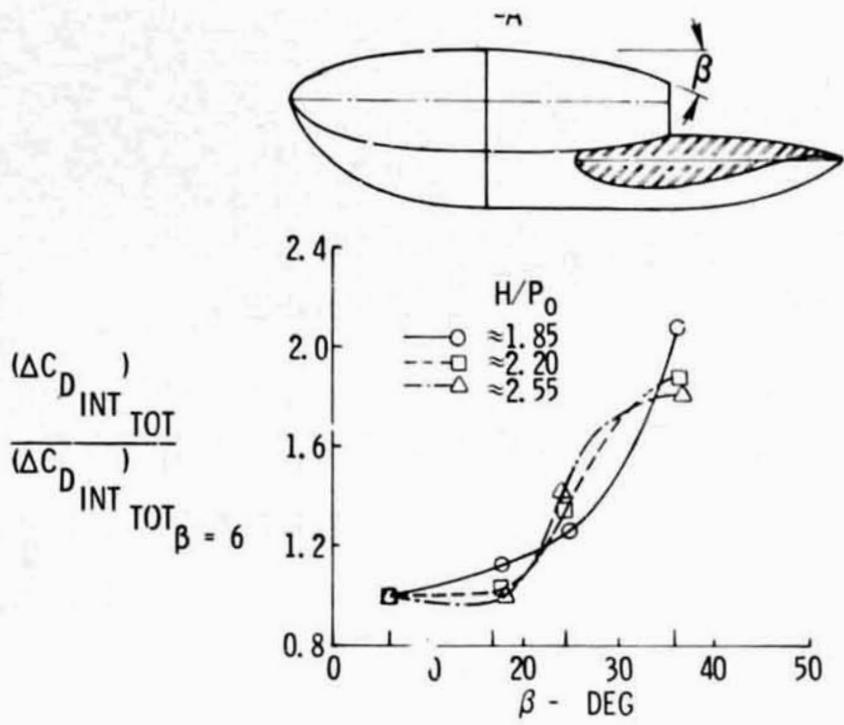
Figure 13.- Effect of nozzle boattail angle on nacelle drag.
Unswept wing; $M_O = 0.68$; $C_{L_A} = 0.40$.
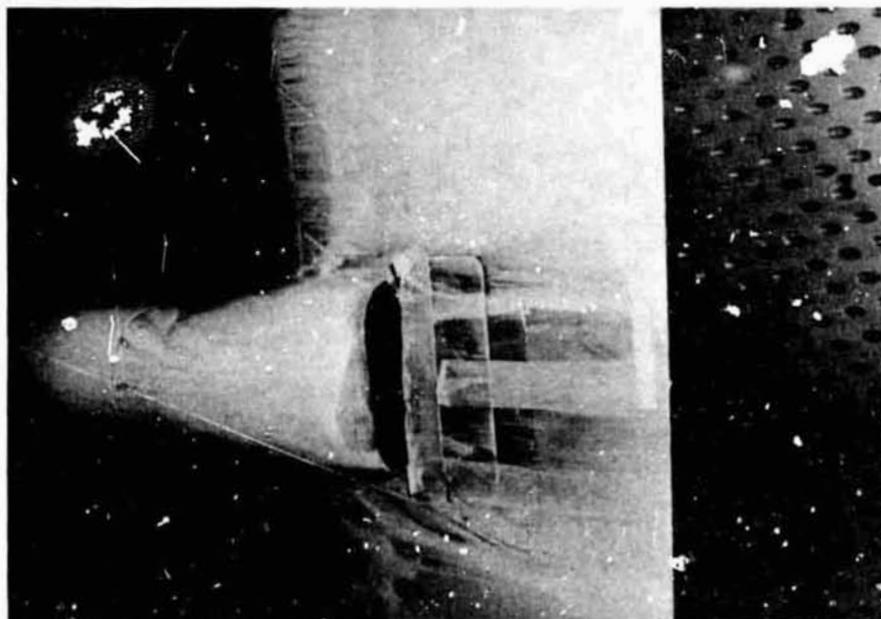

Figure 14.- Boattail separation.

179
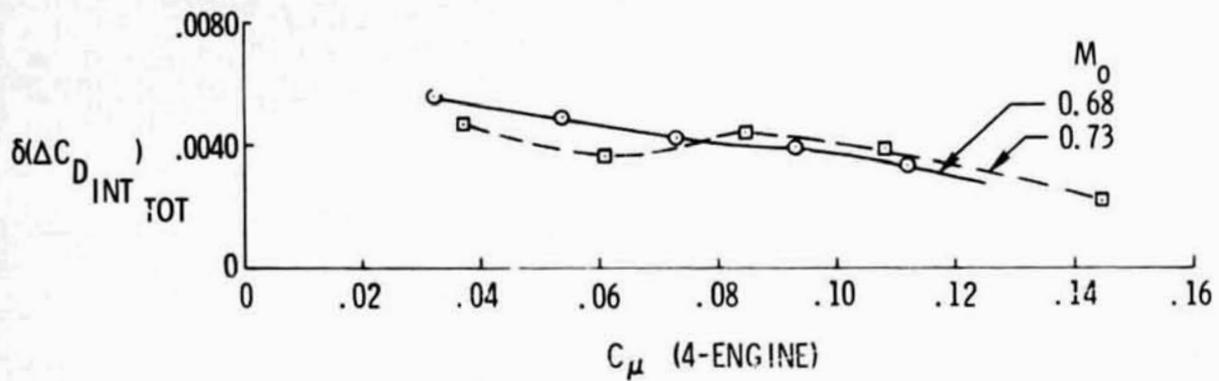
Figure 15.- Effect of multiple engines on interference drag. Swept wing; $(X/c)_{exit} = 0.2$; D-duct nozzles; spacing between nacelles of 2 nacelle diameters.
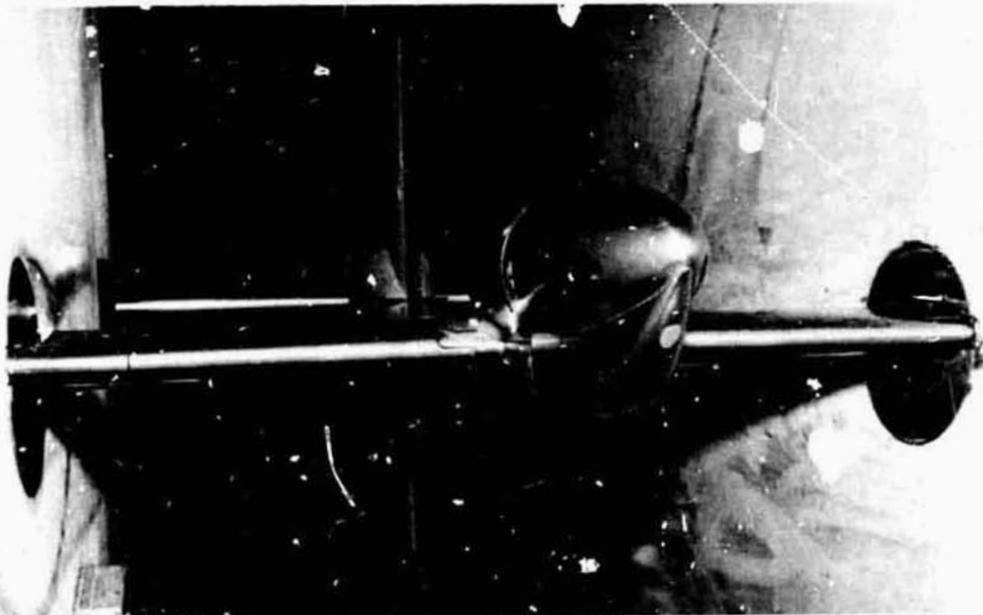

Figure 16.- Wing nacelle pressure model with traversing wake rake.

Hℓ/H

)——— 1.01 > Hℓ/H > 0.99

Hℓ/H
0.99
0.97
0.95
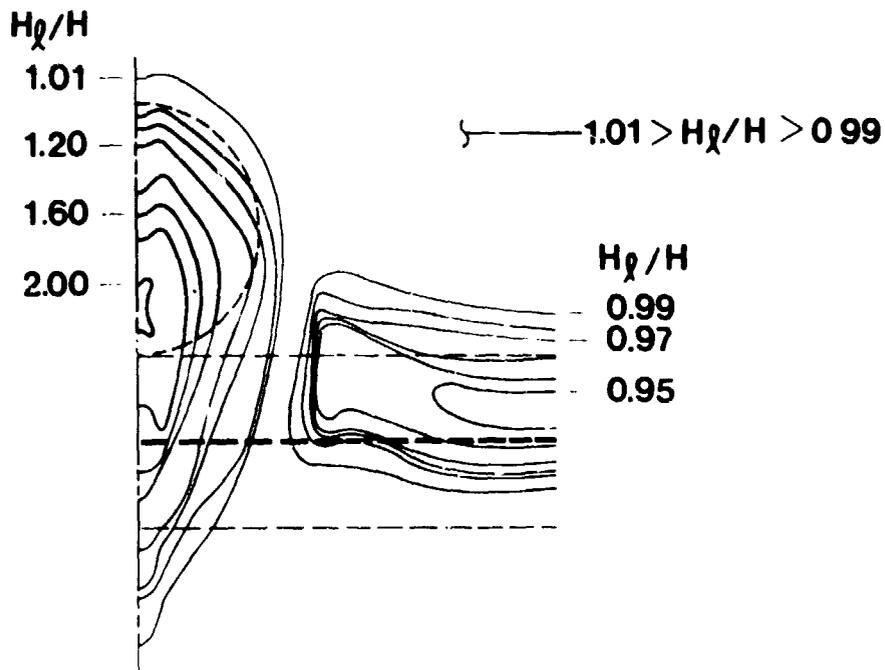
Figure 17.- Wake total pressure pattern. $M_0 = 0.68$;
$\alpha = 2.6°$; $H/P_0 = 2.78$.


O EXPT'L
---- VORTEX LATTICE

C_P

X.c
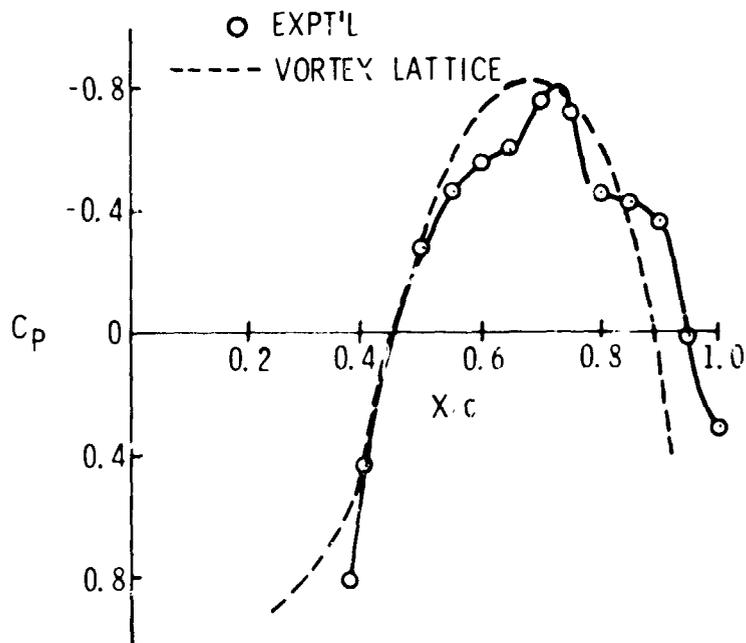
Figure 18.- Comparison of wing surface pressures along jet
centerline of D-duct nacelle with values obtained from
powered vortex-lattice modeling technique $H/P_0 = 2.1$.